Process parameters-weld bead geometry interactions and their influence on mechanical properties : A case of dissimilar aluminium alloy electron beam welds

P.Mastanaiah[1], Abhay Sharma[2], G.Madhusudhan Reddy[3]
[1]Defence Research and Development Laboratory, Kanchanbagh, Hyderabad, India -500058
[2]Indian Institute of Technology Hyderabad, Kandi Campus, Sangareddy, India-502285
[3]Defence Metallurgical Research Laboratory, Kanchanbagh, Hyderabad, India -500058

Abstract

Prediction of weld bead geometry is always an interesting and challenging research topic as it involves understanding of complex multi input and multi output system. The weld bead geometry has a profound impact on the load bearing capability of a weld joint, which in-turn decides the performance in real time service conditions. The present study introduces a novel approach of detecting a relationship between weld bead geometry and mechanical properties (e.g. tensile load) for the purpose of catering the best the process could offer. The significance of the proposed approach is demonstrated by a case of dissimilar aluminium alloy (AA2219 and AA5083) electron beam welds. A mathematical model of tensile braking load as a function of geometrical attributes of weld bead geometry is presented. The results of investigation suggests the effective thickness of weld – a geometric parameter of weld bead has the most significant influence on tensile breaking load of dissimilar weld joint. The observations on bead geometry and the mechanical properties (microhardness, ultimate tensile load and face bend angle) are correlated with detaild metallurgical analysis. The fusion zone of dissimilar electron beam weld has finer grain size with a moderate evaporation and segregation of alloying elements magnesium and copper respectively. The mechanical properties of weld joint are contrlloed by optimum bead geometry and HAZ softening in weaker AA5083 Al alloy.

Key words: Electron Beam Welding, AA2219, AA5083, bead geometry, tensile breaking load

Abbreviations:

EBW	:	Electron Beam Welding
HAZ	:	Heat Affected Zone
T	:	Thickness (mm)
TW	:	Top Width
TD	:	Top Depression
BP	:	Bead Penetration
BW	:	Bead Width
T_e	:	Effective Thickness (mm)
V	:	Accelerating gun Voltage (kV)
I	:	Beam Current (mA)
s	:	Welding Speed (mm/min)
T	:	Thickness of Plate (mm)
R-sq, R^2	:	Coefficient of Determination
SE	:	Standard Error
ANOVA	:	Analysis of Variance

1. Introduction

Electron beam welding (EBW), an autogenous and high power density fusion welding process, is extensively employed in aerospace and defence applications as it offers ample advantages over other conventional arc welding processes. EBW produces welds beads with high depth-to-width ratios, thus, minimizing heat input associated detrimental effects on weld performance [1,2]. As the EBW process is performed in vacuum conditions, fusion related weld defects are, in general, less in electron beam welds as compared to arc welding processes. As reported by Metzer and Lison [3], the electron beam welding has certain unique characteristics such as ability to produce narrow fusion zone with minimum dilution of base materials, ease of precisely locating weld joint etc. make this process as the better choice for fusion welding of dissimilar metals. The serviceability of welded joints mainly depends on shape and size of weld bead and constituent microstructures. By adopting the aforeentioned special charectaristics of the EBW process, it is extensively explored in fusion welding of wide variety of dissimilar metals and alloys[Sun and Karppi,4].

Overview of reported research/State-of-the-art:

In genral, the weld bead geomtry in thick EBW is peculiar- kind of a ‘nail headed’, as shown in Fig. 1. It is difficult to envisage that geometric parameters widely used to define weld bead geometry in other autogenous process like Tungsten inert gas (TIG) welding - top bead width (TW), top depression (TD), bottom penetration (BP), and bottom bead width (BW) [Sharma et al.,5] would effectively explain the behavior of EBW welds. The top and bottom portions of the ‘nail headed’ weld bead are due to different phenomena at surface and inside the body of the workpiecewhich need to be modelled as a two heat source problem [Klykov et al.,6].

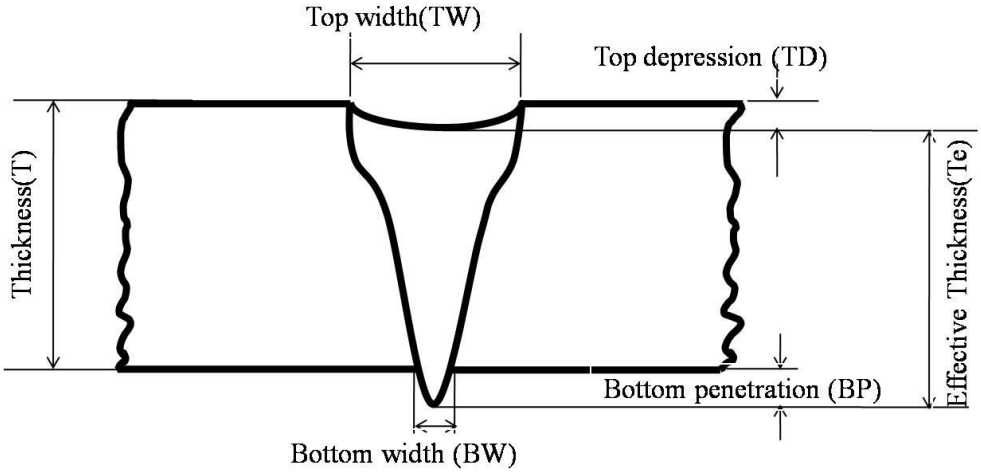

Fig.1. Schematic sketch showing the weld bead geometry of electron beam weld joint

Table 1. Summary of previous investigations on statistical modelling of weld bead geometry

S.No	Researchers, Year	Material, thickness	Design of Experiments	Input parameters	Output parameters
1	Kumar et al.2017 [7]	Ti6Al4V, 5mm	Central composite rotatable design(CCRD)	Laser power, welding speed, de-focused position	Width of fusion zone, width of HAZ and fusion zone area
2	Siddaiah et al.2016 [8]	AISI 304 stainless steel, 2mm	Full factorial design	Accelerating voltage, beam current, welding speed, focus	Weld bead geometry
3	Olshanskaya et al. 2016 [9]	AlMg6 alloy, 20mm	Six-factor three-level nine- run design	Beam current, travel speed, distance between each split beam, impact time of each split beam at each point	Geometric characteristics of weld beads
4	Kanigalpula et al. 2015 [10]	Cu-Cr-Zr alloy,10mm	Central composite design(CCD)	Accelerating voltage, beam current, welding speed, focus	Weld bead geometry
5	Kar et al. 2015 [11]	AISI 304 stainless steel, 15mm	DOE is not followed	Accelerating voltage, beam current, welding speed	Weld bead geometry, HAZ size
6	Dey et al. 2010 [12]	Aluminium 1100, 12mm	Central composite design(CCD)	Accelerating voltage, beam current, welding speed	Weld bead geometry

Therefore very limited investigations are reported for prediction of weld bead geometry shape of EB welds, as shown in Table 1.Most of these works have concentrated on regression analysis or statistical modelling of weld bead geometry, heat affected zone (HAZ) width or in few studies, and joint strength of similar material combinations. Welding of dissimilar alloys deserve more care

and attention as compared to that of similar materials. More so, the weld bead geometry of dissimilar alloys depend on physical and thermal properties of dissimilar base materials and joint strength is also affected by bead geometry as well as the welding parameters.

The present work assumes special significance since no research article is found, to the best of authors' knowledge, in the open literature in which weld bead geometry and its effect on weldmechanical properties pertaining to dissimilar aluminium alloy electron beam weldsare investigated. The alloy combination considered in this investigation is a prominent in aerospace and defence applications. AA2219 aluminium alloy is widely used in manufacturing of airframes, fuel tanks due to its high strength while AA5083 aluminium alloy is employed in pipe lines, external walls of naval sub systems because of its corrosion resistance properties. However in certain applications where some part of subsystem require high strength while the other component may demand for better corrosion resistance, the dissimilar welding between AA2219 and AA5083 aluminium alloys is highly useful. The present work focuses on developing relationship between the weld bead geometry and tensile breaking load of dissimilar aluminium alloy (AA2219 and AA5083) electron beam weld joint. A regression model is developed wherein breaking load is mapped as a function of weld bead geometry. The developed equations are validated through test experiments and further the weld joint strength is correlated to microstructures and distribution of alloying elements in fusion and heat affected zones.

2. Experimental work

The base materials employed in the present research were AA2219-T6 Al-Cu alloy and AA5083-H116 Al–Mg alloy. The analyzed chemical compositions and mechanical properties of base materials are listed in Table.2. The width of weld coupon was maintained along the rolling direction. Electron beam welding of 75 mm width x 125 mm length x 5 mm thickness plates was carried out in square butt joint configuration after positioning and firmly clamping the plates on a CNC work table. The selected welding process parameters that are considered in this study are accelerating voltage(V) in kV, beam current(I) in mA, welding speed(s) in mm/min. Remaining welding conditions such as vacuum level in welding chamber ($1x10^{-4}$mbar), electron gun to work piece distance, focus position and pre-weld cleaning procedures are maintained as constant throughout the experimentation.

Table 2. Chemical composition (%Wt) and mechanical properties of base materials

Base Material	Chemical composition (in % w/w)									Tensile properties			Micro hardness (VHN)
	Cu	Si	Mn	Mg	V	Zn	Ti	Cr	Fe	UTS (MPa)	0.2%YS (MPa)	%El.	
AA2219-T6	5.83	0.03	0.3	---	0.08	0.054	0.04	---	0.1	443	338	10	139
AA5083-H116	--	0.13	0.66	4.2	---	0.01	0.01	0.01	0.3	306	146	20	80

Table 3. L25 orthogonal array along with its experimental results

	Process parameters			**Process outcomes**					
S.No	Voltage (kV)	Current (mA)	Travel Speed (mm/min)	TD	BP	TW	BW	T_e=T-D+BP	Breaking Load in kN
1	40	35	800	0.24	0.04	0.47	0.39	4.8	8.50
2	40	40	900	0.94	0.36	0.81	0.64	4.42	8.95
3	40	45	1000	0.48	0.3	1.4	1.04	4.82	9.16
4	40	50	1100	0.48	0.42	1.53	1.03	4.94	8.46
5	40	55	1200	0.28	0.23	1.3	0.98	4.95	9.04
6	45	35	900	0.46	0.2	1.4	0.86	4.74	8.01
7	45	40	1000	0.3	0.2	0.5	0.38	4.9	8.31
8	45	45	1100	0.4	0.29	1.06	0.76	4.89	8.64
9	45	50	1200	0.5	0.23	1.16	0.90	4.73	8.56
10	45	55	800	0.63	0.45	1.16	1.22	4.82	8.35
11	50	35	1000	0.65	0.66	1.65	0.82	5.01	8.47
12	50	40	1100	0.64	0.63	1.54	0.93	4.99	8.79
13	50	45	1200	0.73	0.12	1.17	0.87	4.39	8.20
14	50	50	800	0.68	0.59	1.35	1.13	4.91	7.91
15	50	55	900	0.87	0.40	1.81	1.35	4.53	7.68
16	55	35	1100	0.57	0.80	2.54	1.01	5.23	9.49
17	55	40	1200	0.83	0.34	1.67	1.14	4.51	9.03
18	55	45	800	1.02	0.81	1.84	1.38	4.79	6.97
19	55	50	900	1.17	0.36	1.58	1.23	4.19	7.47
20	55	55	1000	1.2	0.62	1.76	1.42	4.42	8.06
21	60	35	1200	0.83	0.89	1.70	0.88	5.06	8.02
22	60	40	800	0.95	0.75	2.08	1.47	4.8	7.77
23	60	45	900	1.03	0.56	1.88	1.26	4.53	8.56
24	60	50	1000	0.94	0.41	1.54	1.27	4.47	8.29
25	60	55	1100	1.07	0.25	1.85	1.48	4.18	9.03

Electron beam welding trials were carried out in a CNC controlled low kV electron beam welding machine of M/s.TECHMETA make. The experiments were planned and conducted as per Taguchi method using a L25 orthogonal array with three-factors and each factor with five-levels. The gun to work distance is kept constant at 240mm.The minimum and maximum operating levels of each welding parameter were decided based upon prior experience and after conducting certain pilot experimental bead on trials. Feasible limits of the each parameter was selected in such a way that the resulting electron beam welded joints would have uniform thread-like bottom penetration. The Table.3 shows the number of welding experimental runs and corresponding welding parameters as per L25 orthogonal array.

The weld joints were initially visually inspected and further subjected to X-ray radiography to inspect for the presence of various internal and surface defects. The weld macrostructures of transverse section were examined under optical metallurgical microscope, after standard metallographic sample preparation using modified Keller's reagent.The weld macrostructures were analyzed to measure different weld bead geometrical features such as top bead width (TW), Top depression(TD), bottom penetration (BP) and bottom bead width(BW). The welding parameters and measured weld bead geometry features are given in Table.3.

The tensile test specimens were extracted along the transverse direction of the weld joint such that the specimen geometry conforms to the standard ASTM E8. The room temperature tensile properties of three specimens for each experiment were evaluated in as-welded condition, without machining top depression or penetration, on a universal tensile testing machine of INSTRON make at a crosshead speed of 1 mm/min. A mathematical model was developed using regression analysis - as explained later - for prediction of tensile breaking load of weld joint as a function of weld bead geometrical features.The microhardness was measured using Vickers microhardness tester at 100 gf load. The micro hardness indentations were spaced with 0.25 mm intervals covering various zones of weldments and base materials across the mid thickness of the transverse weld cross section. Face bend testing of weld joint was carried out as per standard ASTM E190. The fractured surfaces of tensile test specimens are examined under ZEISS make scanning electron microscope at an accelerating voltage of 20 kV in order to understand the mode of failure and for the presence of any inter-metallic compound particles on these fracture surfaces.

3. Development of Regression Model

3.1 Regression model

The breakingstrength of a weld bead joint depends on the weld bead geometry and the microstructure of the weld metal and head affected zone. The relation between shape and size of the weld and breaking strength, which is not more often reported, is an important step to understand the weld bead formation and its influence on weld strength. The response parameter representing the tensile breaking load (TBL) of dissimilar electron beam weld joints as a function of weld bead geometrical parameters may be expressed as :

$$TBL = f(T_e, TD, TW, BP, BW) \quad (1)$$

The effective weld thickness $T_e$is as

$$T_e = T - TD + BP \quad (2)$$

A regression equation is developed using stepwise regression method using MINITAB version 17. Detail of this method can be elsewhere [13].The deduced second order polynomial regression equation after incorporating all the values of the regression coefficients is as follows:

$$TBL = 1.7988T_e + 0.724(TD)^2 + 0.263(TW)^2 - 2.621(BP)(BW) \quad (3)$$

For the present case T=5 mm, thus the Eq. (3) can be rewritten using Eq.(2) as follows:

$$TBL = 1.7988\ (5 - TD + BP) + 0.724(TD)^2 + 0.263(TW)^2 - 2.621(BP)(BW) \quad (4)$$

The adequacy of the regression model is judged by the analysis of variance (ANOVA), as shown in Table.4. It is observed that the calculated F- ratio is higher than the tabulated F-ratio at confidence level more than the 95%. So, the developed model is considered to be adequate and predicts the response without appreciable error.

Table 4. Results of analysis of variance for the regression model

Source	Degrees of freedom	Adj Sum Square	Adj Mean Sum square	F-Value	P-Value
Regression	4	1442.67	360.666	1574.27	0.000
Te	1	272.40	272.398	1188.99	0.000
TD*TD	1	1.47	1.472	6.43	0.021
TW*TW	1	1.32	1.323	5.77	0.028
BP*BW	1	4.85	4.853	21.18	0.000
Error	17	3.89	0.229		
Total	21	1446.56			

The model was developed using 21 out of 25 observations and rest four were used to confirm the model. The predicted error for both the development and confirmation data is found within ± 10% band asshown in Fig.2.The coefficients of determination for the mode (R^2, R^2(adj), and R^2(pred)for the observed results are 99.73%, 99.67%, and 99.58%, respectively that shows that the developed model is adequate and can predict the response without appreciable error.

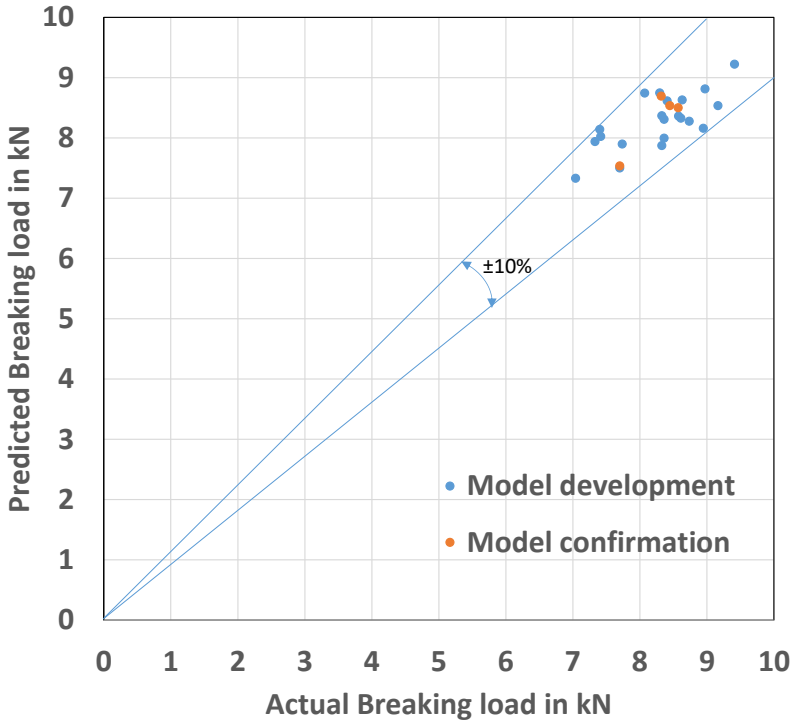

Fig.2. Plot of actual breaking load versus predicted breaking load

The model is further simulated to understand the relationship in between the weld bead geometry and weld strength as presented next. Subsequently the results are corroborated with microstructural observations.

4. Results and discussion

4.1 Weld appearance and bead geometry

The appearance of top and bottom side of a typical weld bead joint and the corresponding X-ray radiograph is shown in Fig.3.The weld joints are noticed to have a depression in fusion zone on top side and a positive penetration at bottom side. X-ray radiograph of weld joints reveals presence of no significant defect.

The appearance of all the dissimilar aluminium alloy electron beam weld cross sections produced with different process parameters is presented in Fig.4. It can be deduced that it is possible to produce defect free weld joints with accelerating voltage 40 to 60kV, beam current 35 to 55mA and welding speed 800 to 1200mm/min. All the weld joints are noticed to be free from bulk porosity but there exists varied weld bead geometries with changes in welding parameters. The weld bead width and top depression is observed to increasing with increase in welding heat input. Overall view of all the weld cross sections reveal presence of certain amount of depression of weld bead zone from top surface and positive penetration is noticed in almost all the weld joints.

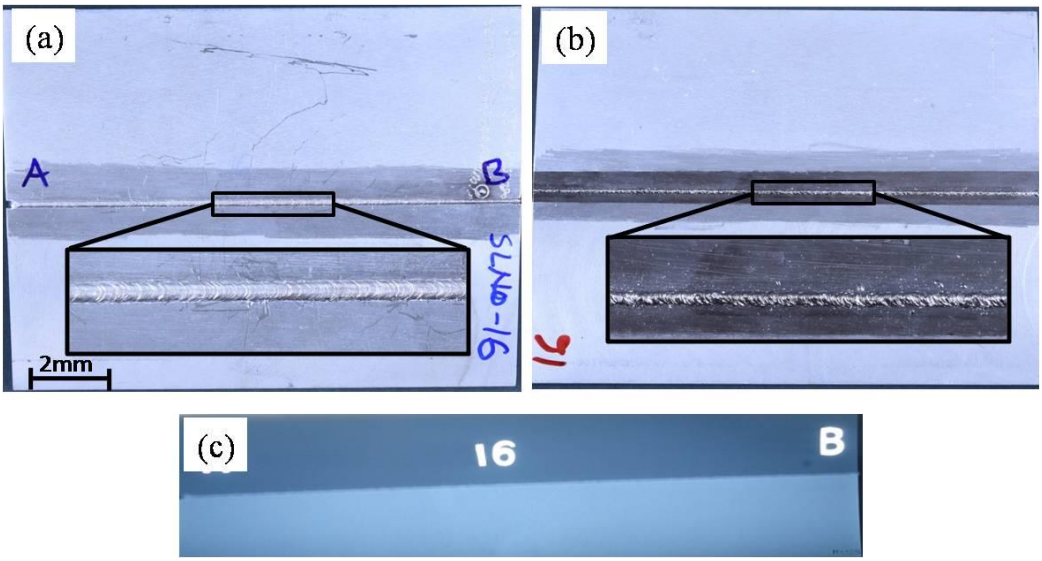

Fig.3 Visual appearance of weld joint (a) top side (b) bottom side (c) X-ray radiograph (accelerating voltage 55kV, beam current 35mA and welding speed of 1100mm/min, gun to work distance of 240mm.)

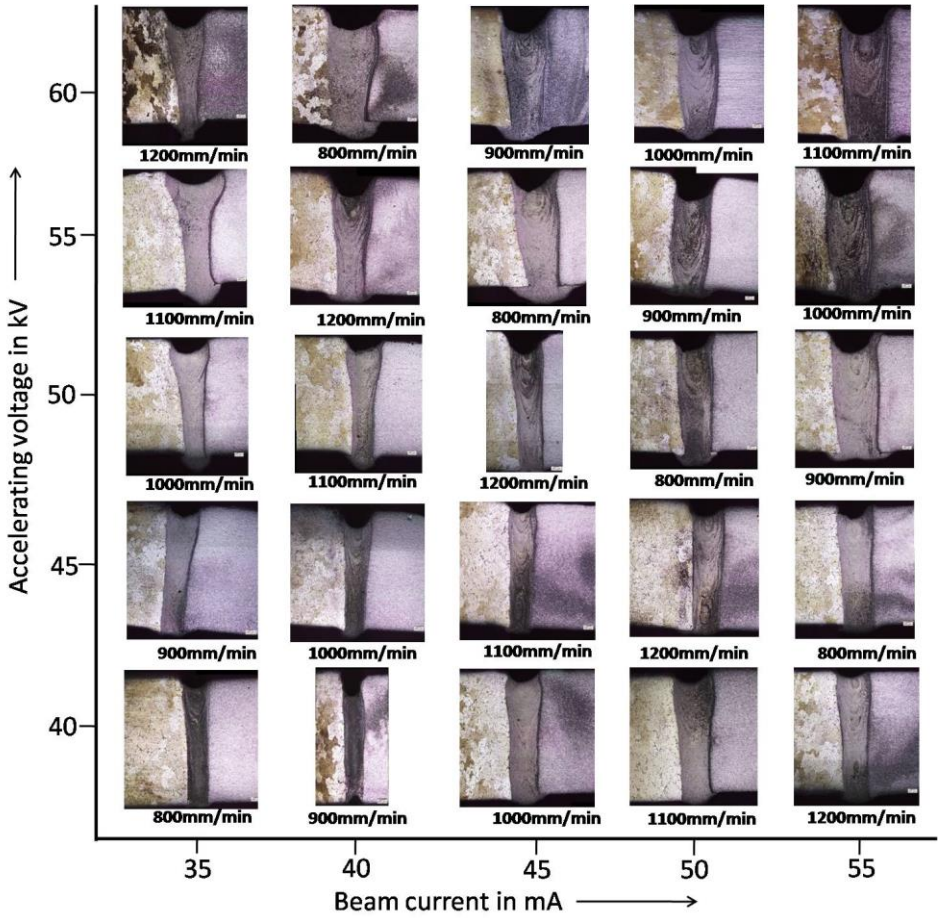

Fig.4 Optical macrographs of the EB weld joints at different welding parameters

4.2 Relationship in between weld bead geometry and weld strength

The weld bead geometrical parameters are interdependent. The interdependence is shown in Fig.5. The change in process conditions that enhance the heat input the volume of molten metal increases, in turn the weld width widens along with deepening of top depression, increase of bottom penetration, and increase in bottom width. However, excess widening of weld width spreads the heat over larger area that reduces the top depression and bottom weld width, as observed in Fig.5. However the molten metal along the center core of the beam increases due to increase in heat input responsible for increasing the weld width.

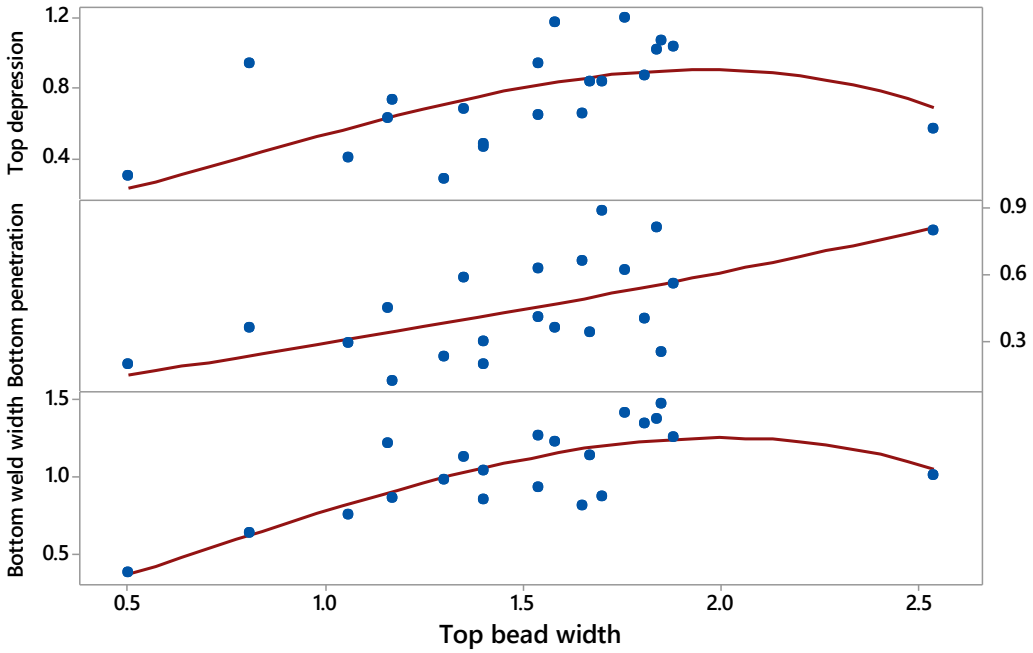

Fig.5 Plots depicting interdependence between weld bead geometrical parameters

The bead geometry influences the weld strength. The relationship between weld bead geometry and breaking load is obtained using simulation of the functional relation in Eq. 4 and shown in Fig.6. It can be seen that with increase in top depression, bottom penetration, and bottom weld width, the breaking load decreases while the process parameters responsible for wider top weld width increases the breaking load. The widening of weld width reduces the top depression at the same time helps to improve bottom penetration. This helps in increase in the total effective weld thickness T_e. The increase in Te increase the weld strength that also corroborates from positive coefficient of T_e in Eq.3. Along with the bead the microstructure - that itself may be affected by weld geometry due to change in heating and cooling rates- also impacts the weld strength as described next.

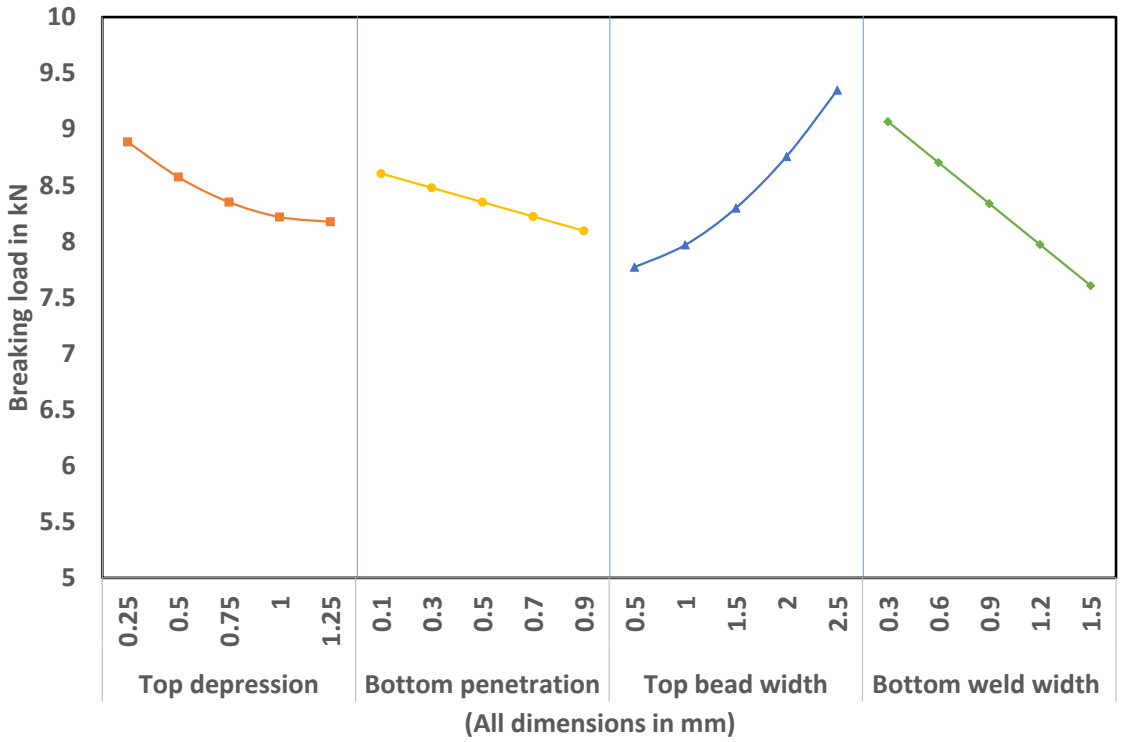

Fig.6. Dependence of breaking load on weld bead geometrical parameters

The macrostructures of two typical weld joints are shown in Fig.7 The macrostructure in Fig.7(a) depicts a weld bead geometry with certain degree of uniformity with minimum amount of top depression and bottom penetration is noticed. Whereas the macrostructure of weld joint shown in Fig.7(b) has relatively highest amount of top depression with an uneven weld bead geometry.

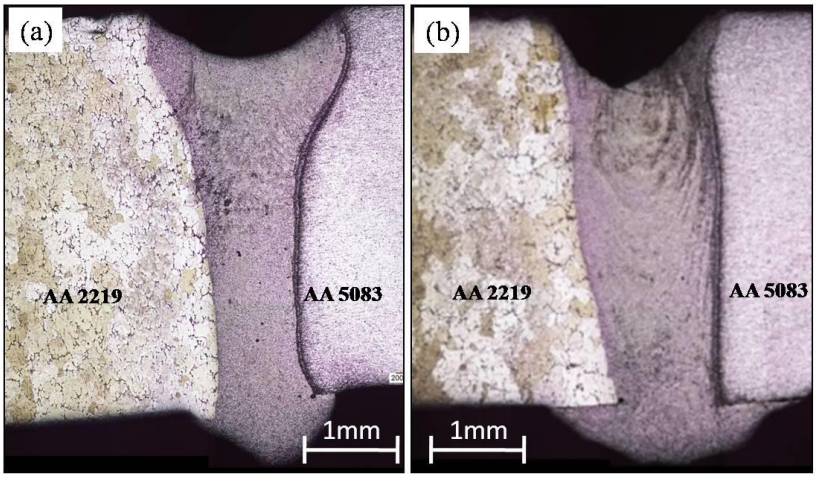

Fig.7 Macrostructures of typical weld joints produced with parameters (a)Accelerating voltage 55kV, beam current 35mA and welding speed 1100mm/min (b)Accelerating voltage 55kV, beam current 45mA and welding speed 800mm/min.

4.3 Microstructural analysis

The optical microstructures of the base materials, AA2219-T6and AA5083-H116 aluminum alloys are shown in Fig.8. The AA2219 base material consists of typical coarse grains measuring approximately to1.5 to 2.0 millimeters with presence θ ($CuAl_2$) particles spread across the whole matrix both at grain boundaries and at interior to the grains.

Precipitation sequence, as mentioned by Li and Schen [14], in a supersaturated solid solution of AA2219 aluminum alloy is as mentioned below.

$$\alpha \rightarrow \alpha + GPzones \rightarrow \alpha + \theta" \rightarrow \alpha + \theta' \rightarrow \alpha + \theta$$

where, α isa solid solution of Cu in Al matrix, GP zones are Guinier-Preston zones.After precipitation hardening or ageing, the alloy attains higher strength due to the impediment of dislocations by $\theta"$ and θ' precipitates. However, the θ-particle is aninter-metallic compound ($CuAl_2$) which stays incoherent to the α-matrix.The microstructure (Fig.8(b)) of AA5083 base material contains uniformly distributed fine grain size with slightly elongated grains in the direction of rolling. It is further observed from Fig.13(a) that the maximum population of grains in AA5083 base material found to be varying from ASTM grain size number from 10 to 12.

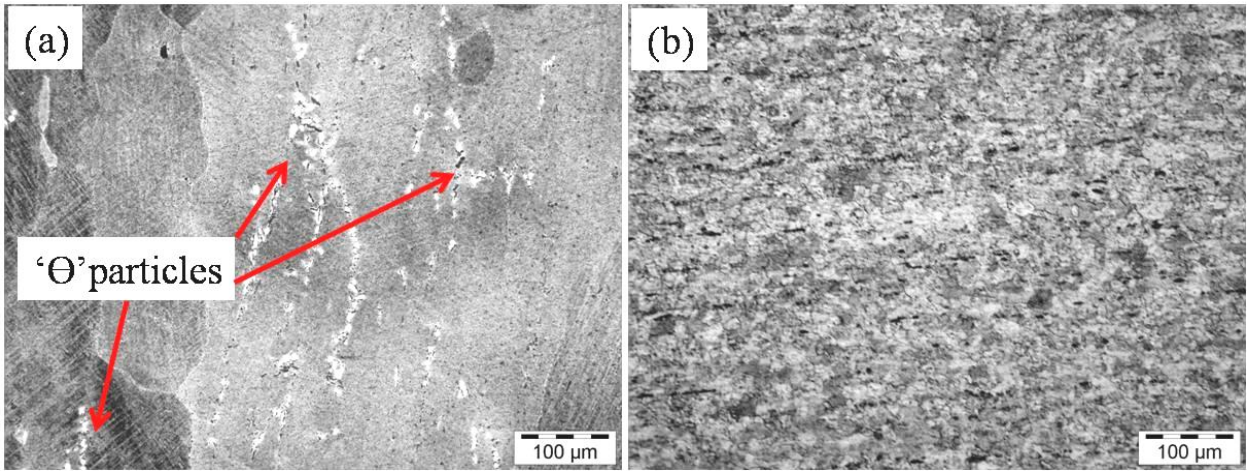

Fig.8Typical optical micrographs of base materials (A) AA2219 (b) AA5083 aluminium alloys

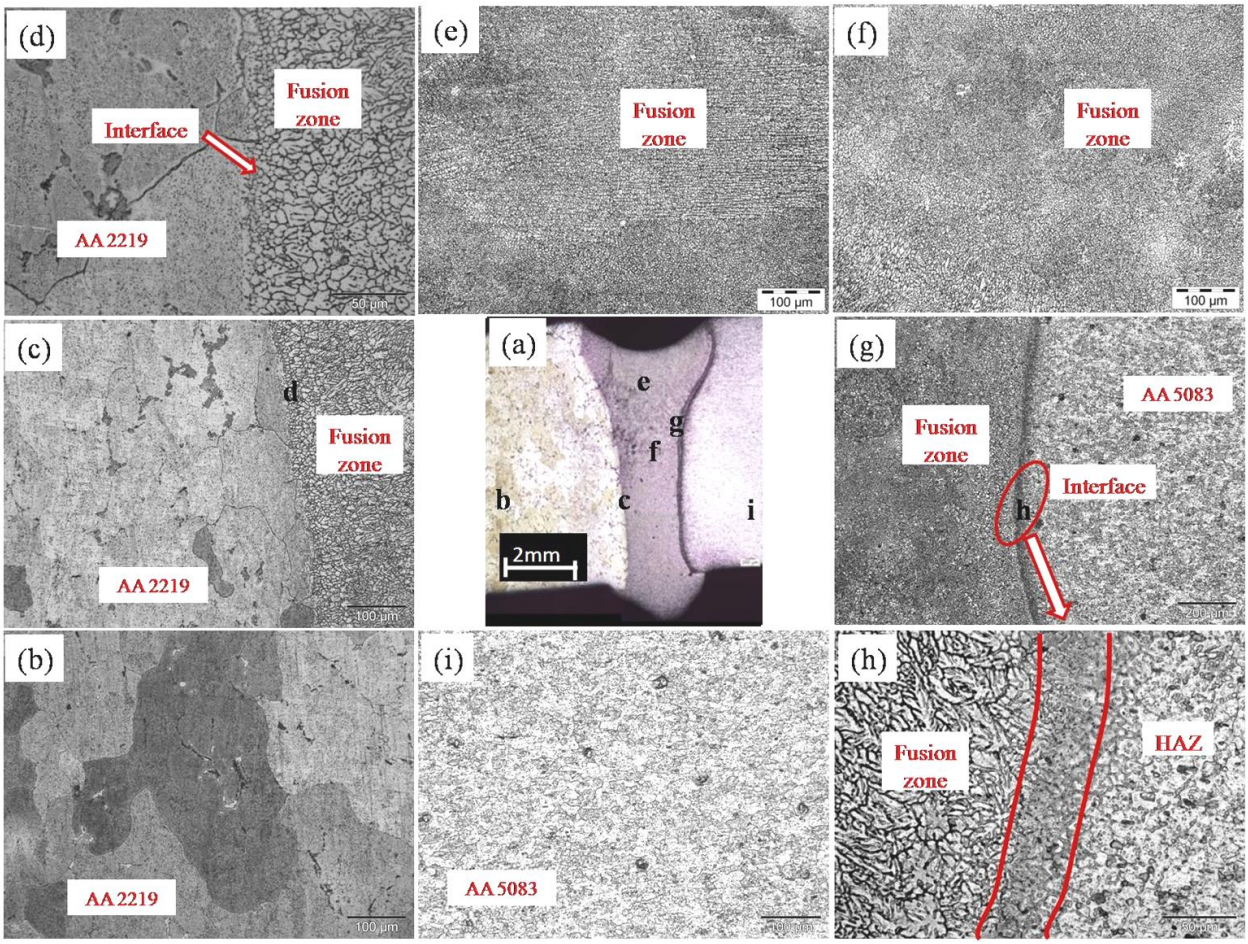

Fig.9Optical microstructures of electron beam weld joint produced with welding parameters (accelerating voltage 55kV, beam current 35mA, welding speed 1100mm/min) (a) macrostructure (b) AA2219 alloy base metal (c)& (d) fusion zone interface at AA2219 alloy side at low and high magnifications respectively (e) & (f) fusion zone at top and mid thickness of cross section (g) &(h) fusion zone interface at AA5083 alloy side at low and high magnifications respectively (i) AA5083 alloy base metal

The microstructures of different zones of a typical electron beam welded joint are shown in Fig.9. The different zones of weld cross-section are marked from b-i. The base metal of AA2219 alloy has coarse as-forged grains as it is seen from Fig.9(b).The microstructures close to AA 2219 interface is shown in Fig.9(c). The interface near AA 2219 alloy side is very clear and distinct, from which the fusion zone grains are noticed to be originated. The grain size in the fusion zone (Fig.9(e)&(f)) is observed to be very fine and is typically smaller by few orders as compared to that of AA 2219 alloy base material. The fine grain size in fusion zone is the result of faster cooling rates prevailing in the key hole mode welding that happens during electron beam welding process. Similar observations on grain size in fusion zone are made by Yan-bin et. al.,[15] and Nair et. al.,[16].The optical microstructures near the both fusion interfaces andfusion zone at higher

magnifications are shown in Fig.10. The fusion zone is found to have primarily very fine columnar dendrites originating from the fusion interface (See Fig.10(a)). The central part of fusion zone consists of equiaxed fine grains (as shown in Fig.10(b)) which are formed due to faster cooling rate that exist during welding.The interface of fusion zone towards AA5083 alloy side is shown in Fig.10(c) and (d). The fusion interface near AA5083 alloy is found to be more diffused over a wide area while the interface at AA2219 alloy side is found to be a sharp line (Fig.10(a)) that is clearly distinct. This phenomenon is due to the fact that the thermal diffusivity of AA 5083 alloy ($0.45cm^2/s$) is smaller than that of AA2219 alloy ($0.5cm^2/s$) which causes major portion of welding heat gets accumulated at the fusion interface of AA5083 alloy instead of getting transferred to the heat affected zone or base material.

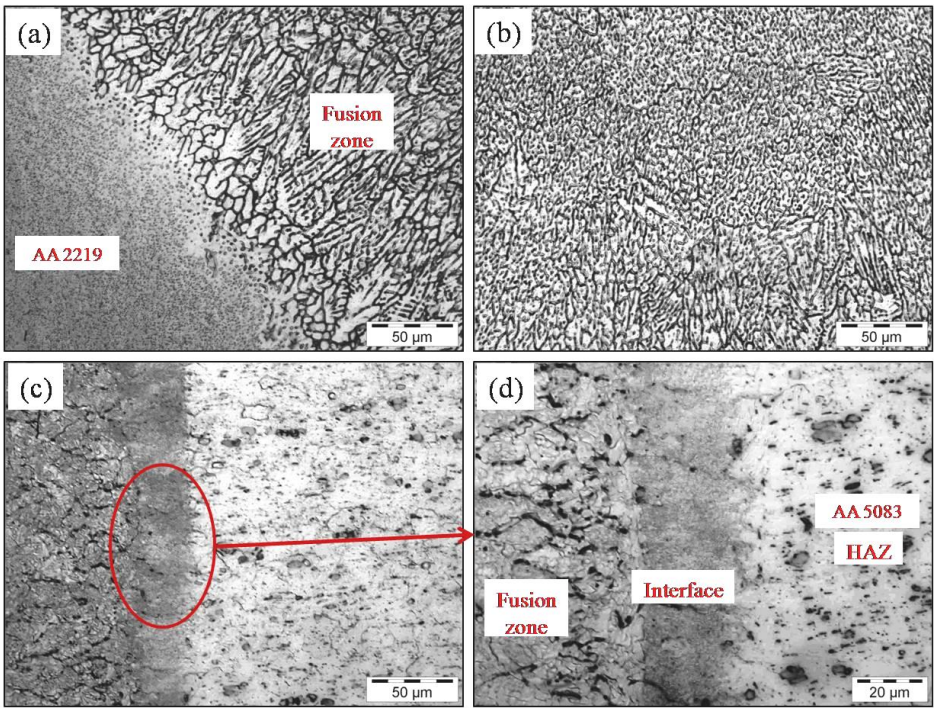

Fig.10 Optical microstructures of (a) fusion interface close to AA2219 alloy side (b) centre of fusion zone (c) &(d) fusion interface close to AA5083 alloy side at two different high magnifications

The optical microstructures given in Fig.11(a) depicts presence of eutectic phase (θ-particles) spread along the grain boundaries of super saturated Al-Cu solid solution in AA2219 aluminium alloy. Upon exposure to the severe welding thermal cycles, re-melting of this prior existing eutectic phase occurs as it is the last to solidify. The grain boundaries close to the fusion interface experience higher degree of temperatures during welding time and these zones are generally very narrow in high energy density welds, mostly covering width of one or two grains. Fig.11(b) clearly indicate eutectic re-melting at the fusion interface near AA2219 alloy side.

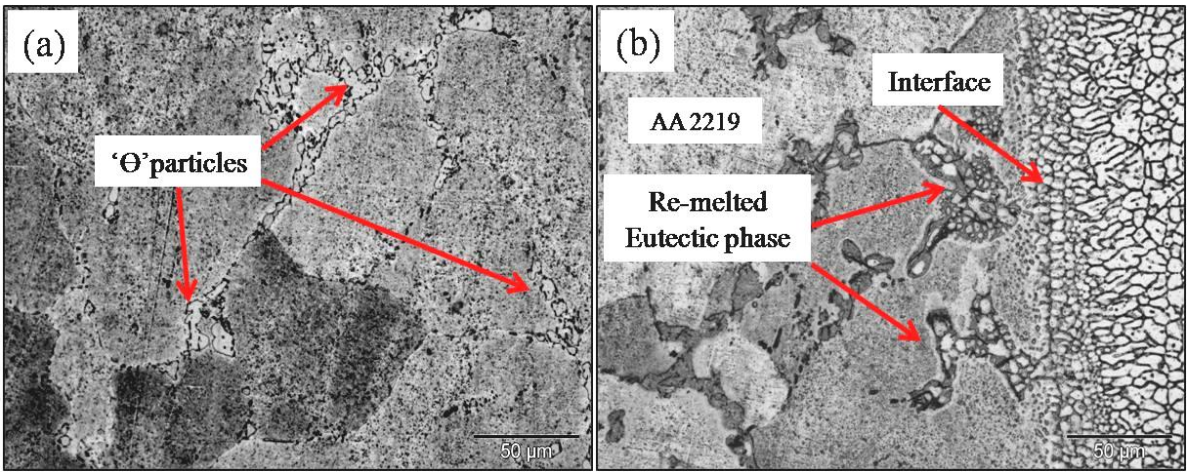

Fig.11 Optical microstructures of (a) AA 2219 alloy base metal showing eutectic phase (θ) (b) fusion interface close to AA2219 alloy showing re-melting of eutectic phase at grain boundaries

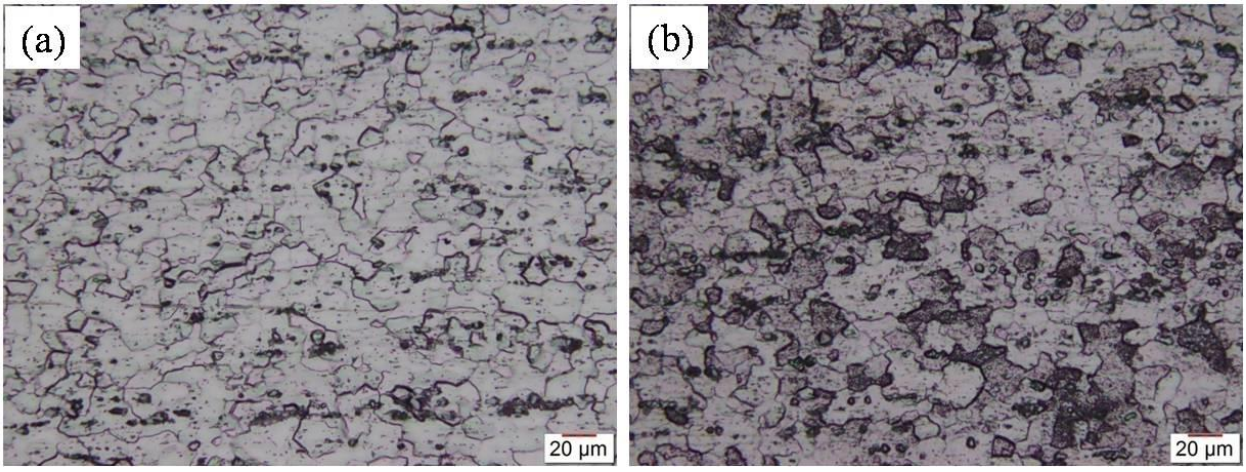

Fig.12 Optical microstructures of (a) AA5083 alloy base material (b) heat affected zone of AA5083 alloy side

High magnification microstructures of AA5083 base material and its corresponding heat affected zone are shown in Fig.12(a)&(b) respectively. The distribution of grain size in base material and HAZ of AA5083 alloy are also measured and plotted (Fig13.(a)&(b)) using planimetric method It is clearly evident from these microstructures and plots that there is very little variation in the grain size of the HAZ as compared to that of base material of AA5083 alloy. This could be primarily due to the prevailing lower welding heat inputs, faster cooling rates and lesser thermal diffusivity of AA5083 alloy.

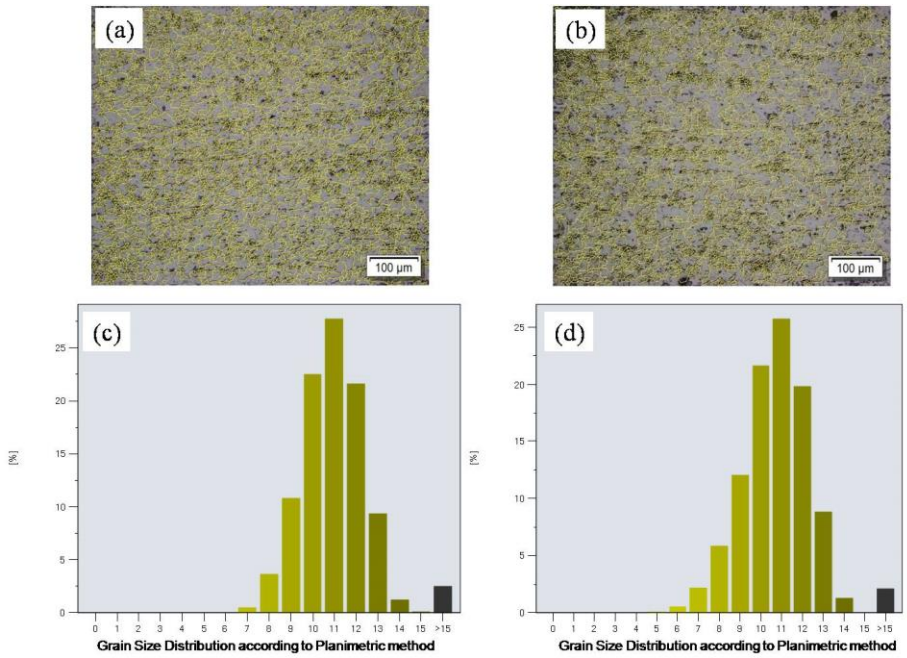

Fig.13 Grain size distribution in (a) AA5083 alloy base metal (b) HAZ of AA2219 alloy (c) &(d) bar chart depicting variation of grain size in AA 5083 base metal and HAZ of AA5083 alloy respectively

Many researchers [15,17 and 18] have reported that the evaporation of major alloying elements during high energy density welding of aluminium alloys. In particular, during laser /electron beam welding of 5xxx aluminium alloys, earlier studies have reported evaporation losses of %Mg even to the extent of 10 to 20%. [19]. In order to understand the composition of existing alloying elements in fusion zone of this dissimilar electron beam weld, EDAX analysis is carried out and the results of area and point analysis are given in Fig.14 and Fig.15. It is noticed from the results of EDAX area analysis given in Fig. that the magnesium is evaporated from the top of fusion zone by 20.2% due to the keyhole mode welding because Mg has low vaporization temperature. In this zone, in addition to 3.35 wt% of magnesium, presence of copper is measured as 3.21wt% which indicates that the sufficient dilution of AA2219 alloy and AA5083 alloy in fusion zone. The wt% of measured copper in this zone is lower than that of AA2219 base material which could be due to the fact that copper segregation in fusion zone. However the EDAX point analysis (Fig.15) in the fusion zone indicates that iron is segregated in fusion zone. Presence of iron along with copper and magnesium in aluminium matrix may lead to formation of fine inter-metallic compounds or precipitates like Al_2CuMg, $Al_{15}Fe_3Si$ etc.

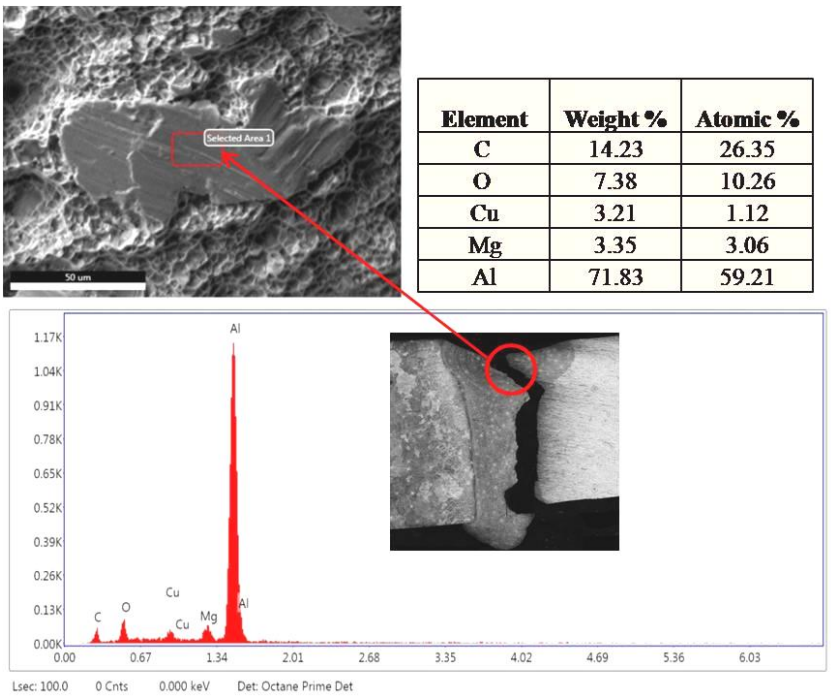

Element	Weight %	Atomic %
C	14.23	26.35
O	7.38	10.26
Cu	3.21	1.12
Mg	3.35	3.06
Al	71.83	59.21

Fig.14 EDAX area analysis of prevailing alloying elements near top of fusion zone

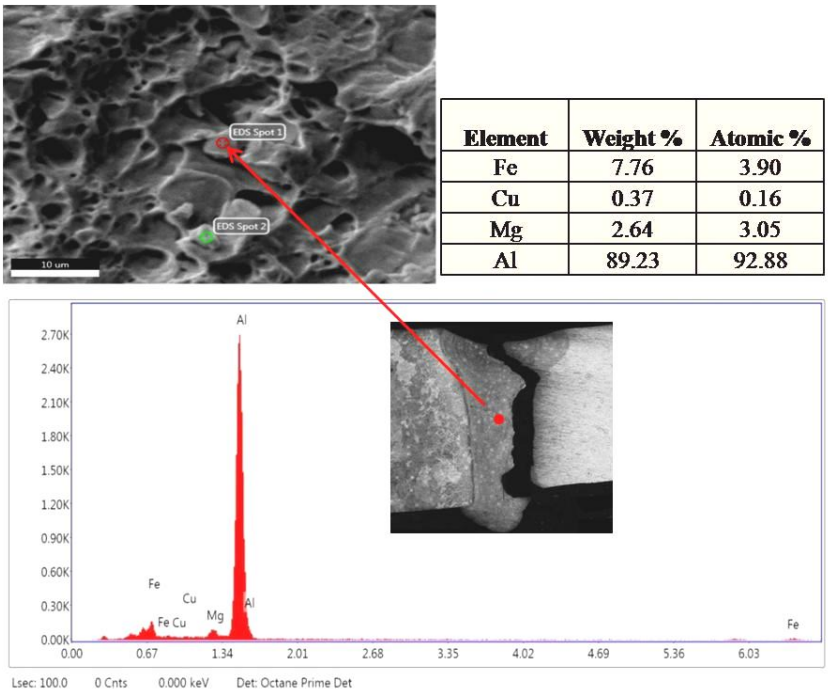

Element	Weight %	Atomic %
Fe	7.76	3.90
Cu	0.37	0.16
Mg	2.64	3.05
Al	89.23	92.88

Fig.15 EDAX point analysis of prevailing alloying elements at a particle in fusion zone

4.4 Microhardness survey

The typical variation of microhardness along the mid thickness of transverse cross section across the dissimilar electron beam weld is shown in Fig.16. The hardness of AA2219 base material was substantially higher than that of AA5083 base material. As can be seen, there was a drop in the hardness in the HAZ close to AA2219 alloy as compared to the un-affected AA2219 base material. A similar trend was observed in HAZ towards AA5083 alloy side as compared to the unaffected AA5083 alloy base material. The hardness of fusion zone was found to be significantly lower than that of AA2219 base material and slightly higher than the AA5083 base material. The reduction in hardness in HAZ of AA2219 alloy side could be due to dissolution or coarsening of Al_2Cu precipitates due to the exposure to welding heat input. Fusion zone hardness is less than that of AA2219 alloy base material due to complete dissolution strengthening precipitates in fusion zone. Similarly the drop in hardness of HAZ of AA 5083 alloy side can be correlated to the loss of cold working / softening due to decreased dislocation density during EB welding process.Yan-bin et al [15], Cam et al [19], Cam et al [20] and Mastanaiah et al [21]have reported reduction of hardness in HAZ of different types 5xxx aluminum alloys.

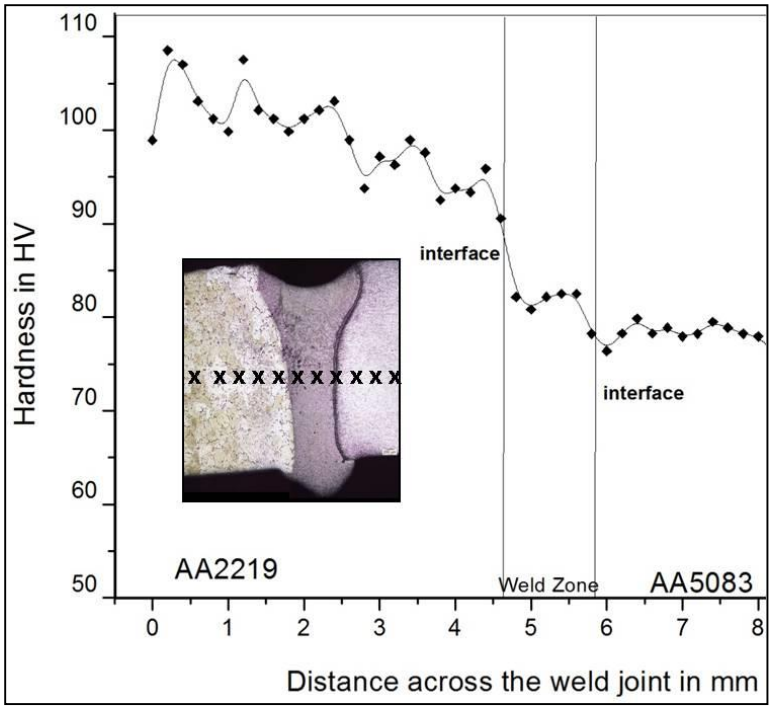

Fig.16 Variation of microhardness across the weld joint at mid thickness

4.5 Tensile test results

The tensile test is conducted with a goal to estimate the load bearing capacity of weld joint in as-welded condition without any post weld machining operations. As the test specimens are not machined or ground after welding, the thickness of the flat transverse tensile test was noticed to be varying beyond acceptable limits as specified by widely practiced standard of tensile testing i.e,

ASTM E8. So testing of tensile specimens, without machining top depression and penetration of the weld joint, has prompted localizing the tensile fracture in fusion zone. So, it was considered to evaluate tensile breaking load and displacement in 25mm gauge length for weld joints instead of usual tensile strength, yield strength and elongations which are dependent of cross sectional area of test specimen.The transverse tensile properties of EB weld joints and the corresponding AA2219 and AA5083 alloy base materials are mentioned in Table.5.Load versus displacement curves for both base materials and weld joint are presented in Fig.17.

One can easily deduce from Fig.17 that the dissimilar weld joint possess the tensile breaking loadmoderately higher than AA5083 alloy base material and less than that of AA2219 alloy base material. The weld specimen has demonstrated better ductility than the specimen of AA2219 alloy base material and slightly lesser than the AA5083 alloy base material.Optical macrograph of the fractured tensile test specimen of weld joints is shown in Fig18. It is clearly evident from the Fig that the fracture of weld joint has initiated from centre of top depression and the crack has propagated through the fusion interface of AA5083 alloy side which posses minimum hardness compared to the other zones of weld joint (Fig.16).

It is noticed that the weld joint fracture was initiated at top of the fusion zone which could be due to stress concentration effect aroused from the profound variations in the weld bead geometry. Top depression of the weld joint has lead to the stress concentration and localization of fracture in fusion zone. Another reason for initiation of crack at the fusion zone could be due to the depletion of major alloying element magnesium from the fusion zone, which was aided by evaporation of magnesium during keyhole mode electron beam welding. Punkari et.al.,[18] and Cam et.al.,[19] have reported loss of magnesium from power beam welding processed weld zones by around 10 to 20%. They also found out that loss of magnesium is one of the major reasons for the fracture initiation at fusion zone of high energy density welding joints of 5xxx aluminium alloys.

However, the dissimilar electron beam weld joint which was welded with parameters 55kV, 35mA and 1100mm/min has shown highest breaking load among all the weld joints. This breaking load is slightly higher tensile breaking load than that of AA5083 alloy base material. One reason for the higher tensile breaking load of weld joint is due to higher effective thickness (5.23mm, as shown in Fig.17) of weld bead which was resulted from the particular welding parameters. In this case, bottom penetration is more than top depression, finally resulting in effective thickness of 5.23mm as against the base material thickness of 5mm. The measured top depression in this particular weld bead geometry suggests that the increase in the breaking load of the dissimilar weld joint as compared to the AA5083 base material could be due to the presence of localized notch like top depression. The presence of notch in a tensile specimen under uni-axial load introduces three effects [22]. (i) There is an increase or concentration of stress at the root of the notch (ii) A tri-axial state of stress is produced at notch (iii) A stress gradient is setup from the root of the notch towards the centre of the specimen. Hence, it is understood that the breaking load of this weld joint is slightly more than that of the AA5083 alloy base material.

The other dissimilar weld joint which was welded with parameters 55kV, 45mA and 800mm/min has demonstrated lowest breaking load among all the weld joints. The ductility of this weld joint possesses lower ductility as compared to other welds. So, the weld is observed to have both breaking load and displacement lower than those of other weld joints.

After initiation fracture, the crack has propagated through the fusion interface of AA5083 alloy side, as this zone has reportedminimum hardness region as compared to all the other regions of dissimilar weldment, which was in turn a resultant of loss of cold working or softening because of exposure to high temperatures caused due to welding heat. A similar observations are reported by Yamaguchi et.al.,[17], Cam et.al.,[19] and Oladimeji et.al.,[23].

Table 5 . Comparison of tensile properties of both base materials and dissimilar EB weld

	Tensile breaking load(kN)	Displacement (mm)	Failure Location
AA2219 Base Material	11.3	2.0	---
AA5083 Base Material	8.1	5.3	---
Dissimilar Electron Beam Weld (55kV, 35mA, 1100mm/min)	9.5	4.6	Fusion zone or interface of AA5083 alloy side
Dissimilar Electron Beam Weld (55kV, 45mA, 800mm/min)	6.9	1.7	Fusion zone

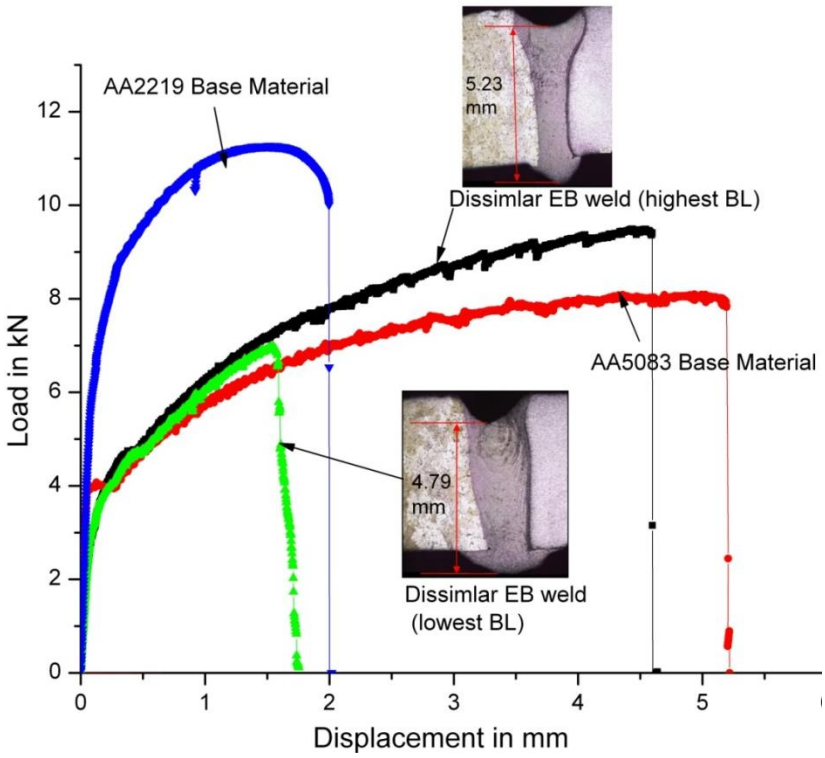

Fig.17 The tensile load versus displacement plots of both base materials and dissimilar EB welds

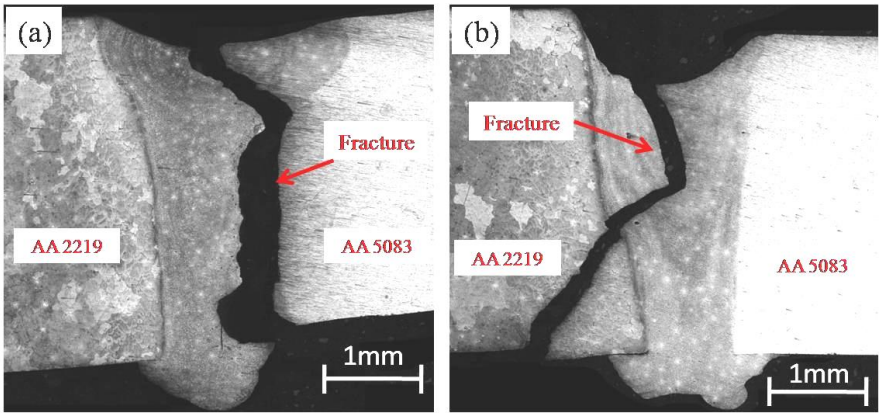

Fig.18 Optical macrograph of fractured tensile test specimensof (a) weld that has highest breaking load (b) weld that has lowest breaking load

4.6 Fractography

The scanning electron microscope (SEM) images of fractured surfaces of tensile test specimens of weld joint of highest breaking load are shown in Fig.19. The fractographs shown in Fig.19 (b)&(c) correspond to the fusion zone and interface on AA5083 alloy side. Fractographs of both the zones primarily portray fine elongated dimples which confirm that fracture has predominantly occurred in ductile mode.

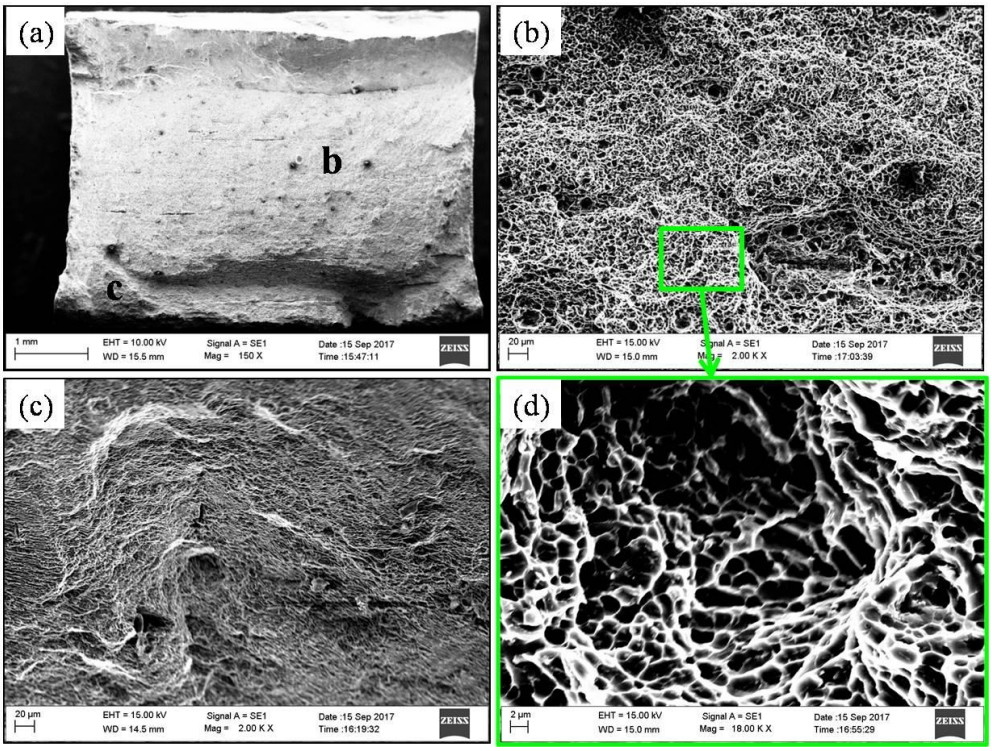

Fig.19 SEM images of fractured surface of tensile test specimen of EB weld with highest breaking load (a) whole fracture surface at low magnification (b), (c) and (d) high magnification fractographs of zones as indicated in (a) &(b)

Fine dimples are characteristic feature of ductile material. The weld joint produced with welding parameters 55kV, 35mA and 1100mm/min has shown highest tensile breaking load and displacement as compared to the welds produced with parameters 55kV, 45mA and 800mm/min and to other weld joints. The dimple size exhibits a directly proportional relationship with tensile breaking load and displacement i.e., if the dimple size is finer, then the tensile breaking load and ductility of the respective weld joint is higher or vice versa.

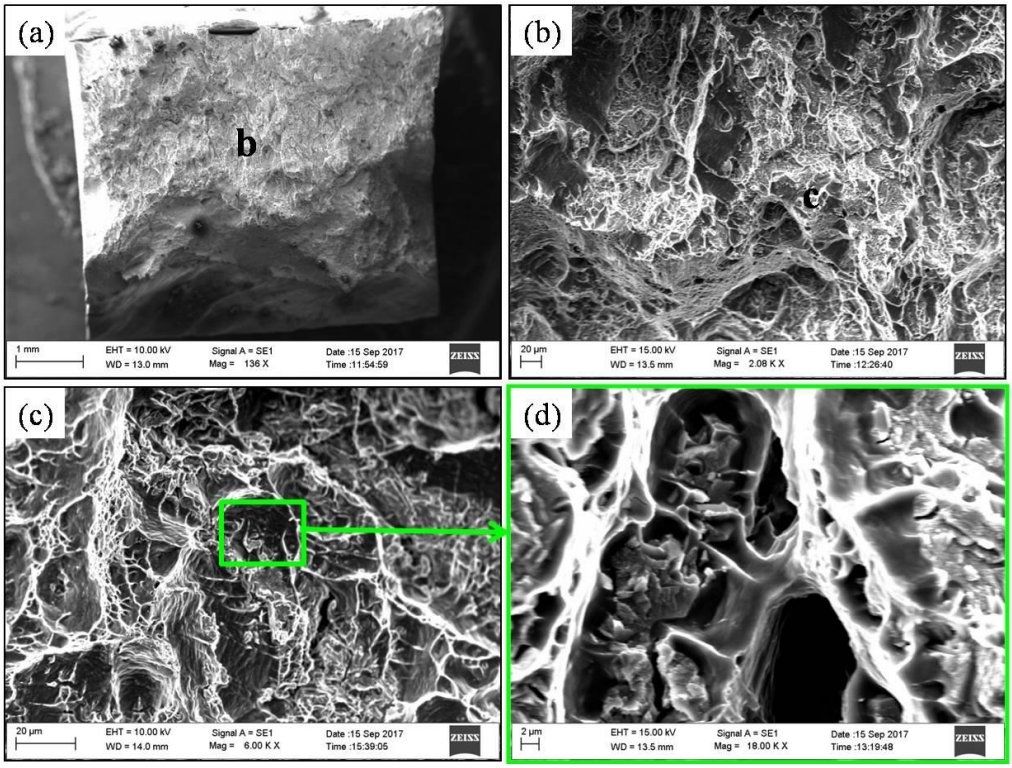

Fig.20.SEM images of fractured surface of tensile test specimen of EB weld with lowest breaking load (a) whole fracture surface at low magnification (b), (c) and (d) high magnification fractographs of zones as indicated in (a) &(b)

The scanning electron microscope (SEM) images of fractured surfaces of tensile test specimens of weld joint of lowest breaking load are shown in Fig.20. The fractographs presented in Fig.20 (b),(c)&(d) suggests that occasional cleavage like features are evident in the grain interiors in addition to the micro void features. The fracture of this particular weld joint appears to be shear dominated phenomenon. The sheared regions were oriented ~45^0 to the tensile stress axis, following a plane of maximum shear stress. This type of shear fracture tends to minimize necking and avoids the tri-axial state of stress that occurs in the necked region.

4.7 Bend test results

The bend tests for the welds joints were conducted mainly to assess the ductility and toughness of weldment. The face bend test samples of dissimilar EB welds before and after bend testing are shown in Fig.21(a)&(b). Fig.21(c)&(d) portrays the bend tested specimens of weld joints that possess highest and lowest breaking load respectively. The bend test specimens are prepared by machining the top depression and bottom penetration of both the weld joints. Face bend test of both the weld joints passed the 90^0 bend angle without resulting in any crack at the root. It is noticed from Fig.21(c)&(d) that the bending has shifted towards AA5083 alloy side as it has relatively lower strength and higher ductility as compared to the weld zone and AA2219 alloy base material.

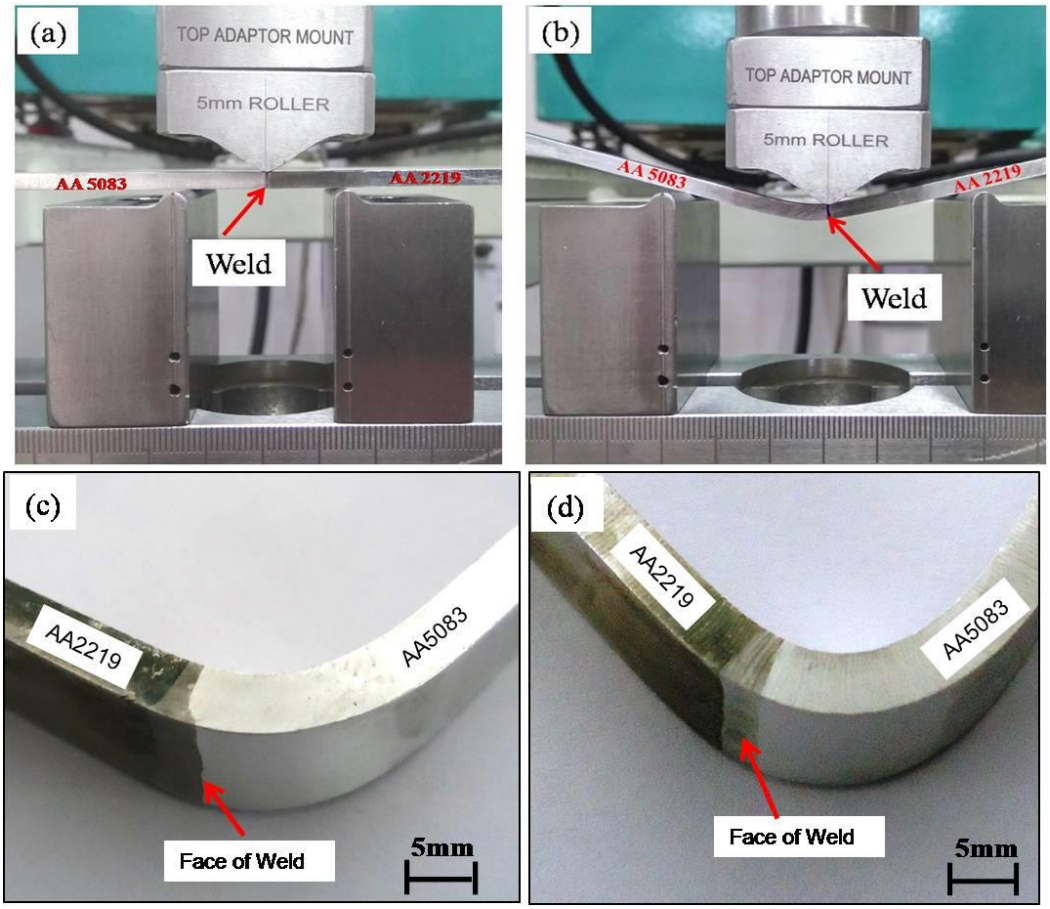

Fig.21 Three point face bend testing of weld joint (a) before bend test (b) during bend test (c) bend tested specimen of weld joint corresponding to highest BL (d) bend tested specimen of weld joint corresponding to lowest BL

5. Conclusions

In the preset work, an in-depth comprehensive metallurgical characterization and the interaction effect of weld bead geometry over performance of electron beam weld joint of dissimilar aluminum alloys (AA2219 and AA5083) was studied. The following conclusions are drawn based on the results of the entire study.

1. Electron beam weld joints of good quality without bulk porosities may be produced over a wide range of welding parameters for the dissimilar combination of AA2219 and AA5083 aluminium alloys. All the joints possess certain amount of top depression and positive penetration.

2. A mathematical model between the weld bead geometry (i.e., top bead width, top depression, bottom penetration, and bottom bead width)and the tensile breaking load of weld joint is developed.The model can predict the tensile breaking load as a function of weld bead geometry as a withinan error of ±10%.
3. The variation in welding parameters that increase the heat input, results in widening of top bead width, deepening of top depression as well as increses in bottom penetration. Weld bead geometry has a major influence on joint strength. Increased top bead width with minimum top depression and maximum bottom penetration leads to increase in effective thickness that in turn results in higher joint strength.
4. The electron beam welding produces very fine grains in fusion zone and softening in HAZ of AA5083 alloy. The key hole mode electron beam welding results in evaporation of magnesium from fusion zone.
5. Fusion interface close to AA5083 alloy has reduced hardness which can be correlated to the loss of cold working / softening due to decreased dislocation density due exposure to severe temperatures caused by welding heat input
6. The dissimilar weld joint possess the tensile breaking load moderately higher than AA5083 alloy base material and less than that of AA2219 alloy base material. The weld specimen has demonstrated better elongation than the specimen of AA2219 alloy base material and slightly lesser than the AA5083 alloy base material. The dissimilar electron beam weld has good bend ductility with major part of deformation existing in softer AA5083 alloy.
7. The failure location of dissimilar electron beam weld is affected by the weld bead geometry and the softening in fusion interface of AA5083 alloy.

Acknowledgements

The financial support from Defence Research and Development Organization (DRDO) is greatly acknowledged. The authors are thankful to Shri.MSR Prasad, Director, Defence Research and Development Laboratory (DRDL) for his continued encouragement and for according permission to publish this work.

References:

1. Scultz H. Electron beam welding. Cambridge: Woodhead Publishing; 2003.
2. Bauer B, Busic M. High energy density welding process. EOLSS Publishers Co Ltd.https://www.eolss.net/Sample-Chapters/C05/E6-171-06-00.pdf
3. Metzer G and Lison R. Electron beam welding of dissimilar metals. The Welding Journal, Welding Research supplement,1976; 230s-240s.
4. Sun Z, Karppi R. The application of electron beam welding for the joining of dissimilar metals: an overview. Journal of Materilas Processing and Technology, 1996;59:257-267.

5. SharmaA, Verma DK, AroraN.A scheme of comprehensive assessment of weld bead geometry.International Journal ofAdvanced Manufacturing Technology,2015;79:5-8; DOI 10.1007/s00170-015-74520.
6. Klykov NA, Dammer AA, Druzhinin AV, Malysh MM. Calculations of the form of the penetration zone in laser welding using a model of two heat sources. Welding International, 1987;1(10):914-916.
7. Kumar C, Das M, Paul CP ,Singh B. Experimental investigation and metallographic characterization of fiber laser beam welding of Ti-6Al-4V alloy using response surface method. Optics and Lasers in Engineering,2017;95:52-68.
8. SiddaiahA, Singh BK, Mastanaiah P. Prediction and optimization of weld bead geometry for electron beam welding of AISI 304 stainless steel. International Journal of Advance Manufacturing Technology, 2017; DOI 10.1007/s00170-016 9046-x.
9. Olshanskaya TV, Salomatova ES, Belenkiy VY, Trushnikov DN, Permyakov GL. Electron beam welding of aluminum alloy AlMg6 with a dynamically positioned electron beam, The International Journal of Advanced Manufacturing Technology,2016;89: 3439–3450.
10. Kanigalpula PKC,Pratihar DK, Jha MN, Derose J, Bapat AV, Pal AR. Experimental investigations, input-output modelingand optimization for electron beam welding of Cu-Cr-Zr alloy plates. International Journal of Advance Manufacturing Technology,2015; DOI 10.1007/s00170-015-7964-7.
11. Kar J, MahantyS, Roy SK, Roy GG. Estimation of average spot diameter and bead penetration usingprocess model during electron beam welding of AISI 304 stainless steel. International Journal of Advance ManufacturingTechnology, 2015;DOI 10.1007/s12666-015-0529-5.
12. Dey V,Pratihar DK,Datta GL,Jha MN,Saha TK,Bapat AV. Optimization and prediction of weldment profile in bead-on-plate welding of Al-1100 plates using electron beam. International Journal of Advance Manufacturing Technology,2010;48:513–528;DOI 10.1007/s00170-009-2307-1.
13. MontgomeryDC, Design and Analysis of Experiments, 8th ed. Newyork:John Wiley & Sons Inc.;2013.
14. Li Bo, SchenY. The investigation of abnormal particle coarsening phenomena in friction stir repair weld of AA2219-T6 aluminium alloy. Materials and Design,2011; 32: 3796-3802.
15. Yan-bin C, Yu-gang M, Li-qun LI, Lin WU. Joint performance of laser-TIG double-side welded 5A06 aluminum alloy. Transactions of Nonferrous Metals Society of China,2009; 19: 26-31.
16. Nair BS, Phanikumar G, Prasad Rao K, Sinha PP. Improvement of mechanical properties of gas tungsten arc and electron beam welded AA2219 (Al-6 wt-%Cu) alloy. Science and Technology of Welding and Joining, 2007; 579-585.

17. Yamaguchi T, Kato M, Nishio K. Metallurgical charateristics of A5083-O aluminium alloy welded by high energy density welding. Welding International, 2010;13(9):712-720.
18. Punkari A, Weckman DC, Kerr HW. Effects of magnesium content on dual beam Nd:YAG laser welding of Al-Mg alloys. Science and Technology of Welding and Joining,2003;8:269-281.
19. Cam G, Ventzke V, Santos JFD, Kocak M, Jennequin G, Gonthier-Maurin P. Characterisation of electron beam welded aluminium alloys. Science and Technology of Welding and Joining,1999;4:317-323.
20. Cam G, Ipekoglu G. Recent developments in joining of aluminum alloys. International Journal of Advance Manufacturing Technology, 2016; DOI 10.1007/s00170-016-9861-0.
21. Mastanaiah P,Sharma A, Reddy GM. Dissimilar Friction Stir Welds in AA2219-AA5083 Aluminium Alloys: Effect of Process Parameters on Material Inter-Mixing, Defect Formation, and Mechanical Properties. Transactions of the Indian Institute of Metals, 2016; 69 (7):1397-1415. ISSN 0972-2815.
22. Hetzberg RW. Deformation and fracture mechanics of engineering materials, 2nd ed.London: John Wiley & Sons Inc, London;1983.
23. Oladimeji OO, Taban E. Trend and innovations in laser beam welding of wrought aluminium alloys. Welding in the World, 2016; DOI 10.1007/s40149-016-0317-9.